Title

Photoreceptors in a mouse model of Leigh syndrome are capable of normal light-evoked signaling.

Journal

Journal of Biological Chemistry, 294(33)

Authors

Gospe, Sidney
Travis, Amanda
Kolesnikov, Alexander
et al.

Publication Date

2019-08-16

DOI

10.1074/jbc.RA119.007945

Peer reviewed

Photoreceptors in a mouse model of Leigh syndrome are capable of normal light-evoked signaling

Received for publication, February 27, 2019, and in revised form, June 12, 2019 Published, Papers in Press, June 27, 2019, DOI 10.1074/jbc.RA119.007945

Sidney M. Gospe III[‡1], Amanda M. Travis[§2], Alexander V. Kolesnikov[¶], Mikael Klingeborn[‡], Luyu Wang[‡], Vladimir J. Kefalov[¶], and Vadim Y. Arshavsky[‡§]

From the Departments of [‡]Ophthalmology and [§]Pharmacology and Cancer Biology, Duke University, Durham, North Carolina 27710, and [¶]Department of Ophthalmology and Visual Sciences, Washington University School of Medicine, Saint Louis, Missouri 63110

Edited by Paul E. Fraser

Mitochondrial dysfunction is an important cause of heritable vision loss. Mutations affecting mitochondrial bioenergetics may lead to isolated vision loss or life-threatening systemic disease, depending on a mutation's severity. Primary optic nerve atrophy resulting from death of retinal ganglion cells is the most prominent ocular manifestation of mitochondrial disease. However, dysfunction of other retinal cell types has also been described, sometimes leading to a loss of photoreceptors and retinal pigment epithelium that manifests clinically as pigmentary retinopathy. A popular mouse model of mitochondrial disease that lacks NADH:ubiquinone oxidoreductase subunit S4 (NDUFS4), a subunit of mitochondrial complex I, phenocopies many traits of the human disease Leigh syndrome, including the development of optic atrophy. It has also been reported that *ndufs4*$^{-/-}$ mice display diminished light responses at the level of photoreceptors or bipolar cells. By conducting electroretinography (ERG) recordings in live *ndufs4*$^{-/-}$ mice, we now demonstrate that this defect occurs at the level of retinal photoreceptors. We found that this deficit does not arise from retinal developmental anomalies, photoreceptor degeneration, or impaired regeneration of visual pigment. Strikingly, the impairment of *ndufs4*$^{-/-}$ photoreceptor function was not observed in *ex vivo* ERG recordings from isolated retinas, indicating that photoreceptors with complex I deficiency are intrinsically capable of normal signaling. The difference in electrophysiological phenotypes *in vivo* and *ex vivo* suggests that the energy deprivation associated with severe mitochondrial impairment in the outer retina renders *ndufs4*$^{-/-}$ photoreceptors unable to maintain the homeostatic conditions required to operate at their normal capacity.

Mitochondria house the enzymatic machinery for oxidative phosphorylation (OX-PHOS)[3] and serve as the major source of cellular ATP production in most eukaryotic cells. Although mitochondrial DNA (mtDNA) encodes a minority of the subunits of OX-PHOS protein complexes, most subunits are encoded by the cell's nuclear DNA and trafficked post-translationally to the mitochondria (1). Disruption of the enzymatic reactions of OX-PHOS not only reduces the efficiency of ATP production but also leads to an increase in reactive oxygen species, which destabilize the mitochondrial genome and damage proteins and lipids throughout the cell, potentially leading to apoptosis (2). Retinal neurons are highly sensitive to mitochondrial dysfunction. Inherited deficiencies in mitochondrial OX-PHOS enzymes may result in vision loss, often due to death of retinal ganglion cells (RGCs) and subsequent atrophy of the optic nerve, which comprises RGC axons (3). Disease of the outer retina in the form of pigmentary retinopathy has also been described in some forms of mitochondrial disease, but whether this reflects a primary pathology of the retinal photoreceptors or of supporting retinal pigment epithelium (RPE) cells is uncertain (4, 5).

The severity of human disease related to mitochondrial dysfunction is highly variable. On one end of the spectrum is Leber hereditary optic neuropathy (LHON), which is among the most common human diseases with a mitochondrial inheritance pattern (6). Although it causes severe vision loss from optic atrophy, systemic manifestations are rare, and patients can typically expect to have a normal lifespan (5). Most LHON cases result from hypomorphic mutations in mtDNA encoding three of the 14 core subunits of complex I of OX-PHOS (ND1, ND4, and ND6) and reducing complex I catalytic activity to varying degrees (7, 8). At the other end of the mitochondrial disease spectrum is Leigh syndrome, a rare neurometabolic disease manifesting as hypotonia and ataxia in early childhood, with progressive cardiac and respiratory failure often leading to death within a few years of life (9). Visual impairment secondary to optic atrophy and pigmentary retinopathy is commonly noted during infancy (10). Some mutations associated with

This work was supported by NEI, National Institutes of Health Grants EY028610 (to S. M. G.), EY022959 (to V. Y. A.), EY025696 and EY027387 (to V. J. K.), and Core Grants EY005722 (to Duke University) and EY002687 (to Washington University) as well as a Duke University School of Medicine Strong Start award (to S. M. G.) and an unrestricted Research to Prevent Blindness grant (to Duke Eye Center). The authors declare that they have no conflicts of interest with the contents of this article. The content is solely the responsibility of the authors and does not necessarily represent the official views of the National Institutes of Health.

[1] To whom correspondence should be addressed. Tel.: 919-681-9191; Fax: 919-684-0547; E-mail: sid.gospe@duke.edu.

[2] Present address: Dept. of Ophthalmology and Visual Sciences, University of Michigan, Ann Arbor, MI 48105.

[3] The abbreviations used are: OX-PHOS, oxidative phosphorylation; NDUFS4, NADH:ubiquinone oxidoreductase subunit S4; ERG, electroretinography; LHON, Leber hereditary optic neuropathy; mtDNA, mitochondrial DNA; RPE, retinal pigment epithelium; RGC, retinal ganglion cell; cd, candela(s); P, postnatal day; PKC, protein kinase C; CNG, cyclic nucleotide–gated cation channel; ChAT, choline acetyltransferase; R_{max}, maximal response amplitude; $I_{0.5}$, half-saturating light intensity.

Leigh syndrome affect subunits of complex I, and they likely produce more profound dysfunction of the enzyme complex than those mutations associated with LHON (11).

Genetic mouse models of complex I dysfunction have produced phenotypes similar to their human counterparts, also demonstrating a dependence on the severity of OX-PHOS impairment. For instance, a mouse line carrying a hypomorphic P25L mutation in the ND6 subunit of complex I resulting in ~30% reduction in complex I activity had no reduction in lifespan but demonstrated a delayed RGC degeneration phenotype manifesting by 24 months of age (12). In contrast, a mouse line with a deletion of the accessory complex I subunit encoded by the nuclear gene *ndufs4* demonstrated severe systemic pathology due to profound instability of complex I as a whole (13). Similar to Leigh syndrome patients harboring *ndufs4* mutations, homozygous *ndufs4*$^{-/-}$ mice developed a rapidly progressive myoencephalopathy, with animal death commencing around postnatal day 50 (P50). Although these mice have normal RGC counts initially, RGC degeneration was found to begin prior to death of the mice (14). Interestingly, both of these mutant mouse models were reported to demonstrate abnormal electroretinography (ERG) responses, suggesting pathology of preganglionic retinal neurons. However, histologic analysis of the outer retina has not yet been described, and it is unclear whether photoreceptor degeneration is a feature of these mouse models of complex I deficiency. We now demonstrate that the retinal signaling anomalies observed in *ndufs4*$^{-/-}$ mice can be completely rescued by altering the retinal extracellular environment and, therefore, are not due to irreversible photoreceptor dysfunction but rather to abnormal homeostatic conditions in the outer retina.

Results

ndufs4$^{-/-}$ *mice produce abnormal in vivo ERG responses*

Retinas from *ndufs4*$^{-/-}$ mice have previously been shown to have >80% reduction in complex I activity and a corresponding severe reduction in oxidative metabolism (14). The impact of this metabolic deficiency on retinal signaling has been assessed by analyzing ERG b-waves, which were profoundly reduced (13, 14). As the recordings had been performed as early as P21, this raised the question of whether lack of NDUFS4 resulted in aberrant retinal development or an early degenerative process. To explore these possibilities, we performed comprehensive *in vivo* ERG analysis of *ndufs4*$^{-/-}$ mice and their WT littermates at multiple ages (Fig. 1). Light responses were recorded from dark-adapted mice (Fig. 1*A*) and in the presence of 30 cd/m^2 illumination saturating rod responses (Fig. 1*B*). The data were fit using a double-hyperbolic function as in Herrmann *et al.* (15) (Table 1). In contrast to the findings of Kruse *et al.* (13), we observed robust ERG b-waves in P22 *ndufs4*$^{-/-}$ mice under both scotopic and photopic conditions. The b-wave amplitudes were modestly reduced compared with WT, although this difference did not reach statistical significance at most flash intensities (Fig. 1*C*). Similarly, modest reductions in the amplitude of the ERG a-wave and in the responses to flashes in the presence of rod-saturating light were observed in *ndufs4*$^{-/-}$ mice at P22. These amplitude reductions were more pronounced at P36 (Fig. 1*D*) and then appeared to plateau, showing a similar reduction at age P47, the last time point tested within the lifespan of the mice (Fig. 1*E*). The average maximal ERG b-wave and a-wave responses at P36 and P47 in *ndufs4*$^{-/-}$ mice were all roughly half of the maximal responses in the WT littermates (Table 1).

ndufs4$^{-/-}$ *mice display normal outer retina morphology without degeneration*

Because ERG a-waves originate from photoreceptors and b-waves reflect primarily downstream responses of ON-bipolar cells, the proportionate reduction of ERG a- and b-wave amplitudes observed in *ndufs4*$^{-/-}$ mice of all ages points to a signaling abnormality at the level of photoreceptors. This could either be due to abnormal phototransduction or to a reduction of the total number of photoreceptors. Morphological analysis of *ndufs4*$^{-/-}$ retinas by light and EM revealed healthy appearing photoreceptors with well-ordered outer segments at all ages, indicating no deficiency in outer segment morphogenesis or maintenance (Fig. 2, *A* and *B*). Furthermore, expression of several representative outer segment proteins participating in or regulating rod phototransduction was unchanged in *ndufs4*$^{-/-}$ retinas compared with WT (Fig. 2*C*). We also confirmed proper compartmentalization of rod photoreceptors, as rhodopsin and the β1-subunit of the cyclic nucleotide–gated channel (used as representative proteins of outer segment discs and plasma membrane, respectively) retained their normal localization in *ndufs4*$^{-/-}$ retinas, whereas the inner segment marker Na^+/K^+-ATPase remained excluded from outer segments (Fig. 2*D*).

Consistent with the lack of gross morphological abnormalities, there was no evidence of photoreceptor degeneration, as the number of photoreceptor nuclei within the outer nuclear layer in *ndufs4*$^{-/-}$ mice was unchanged compared with WT littermates, even at P47 (Fig. 3*A*). Furthermore, there was no significant difference in mean outer segment length at this late time point ($p = 0.60$; Fig. 3*B*). It has been reported that rod bipolar cells are the first retinal neurons to degenerate in *ndufs4*$^{-/-}$ mice (16), which could theoretically explain the reduction in ERG b-wave amplitudes, at least under scotopic conditions. However, in contrast to this previous report, when we immunolabeled retinal cross-sections at P49 with the rod bipolar cell marker PKC-α, no difference was found in rod bipolar cell count between *ndufs4*$^{-/-}$ and WT retinas ($p = 0.71$; Fig. 3*C*). This lack of detectable rod bipolar cell pathology further supports our conclusion that the ERG defect in *ndufs4*$^{-/-}$ mice originates primarily from photoreceptors. We confirmed a previously reported reduction in the number of choline acetyltransferase–positive starburst amacrine cells in *ndufs4*$^{-/-}$ retinas ($p < 0.01$; Fig. 3*D*) (14). However, prior ERG analysis of mouse retinas in which starburst amacrine cells were ablated revealed no effect on a-wave amplitude and minimal effect on b-wave amplitude (≤10% reduction and only at the highest stimulus intensities) (17). Thus, loss of starburst amacrine cells would seem to contribute little to the decreased ERG amplitudes of *ndufs4*$^{-/-}$ mice.

Because degeneration of preganglionic retinal neurons did not appear to explain the electrophysiology phenotype of *ndufs4*$^{-/-}$ mice, we asked whether these findings could be

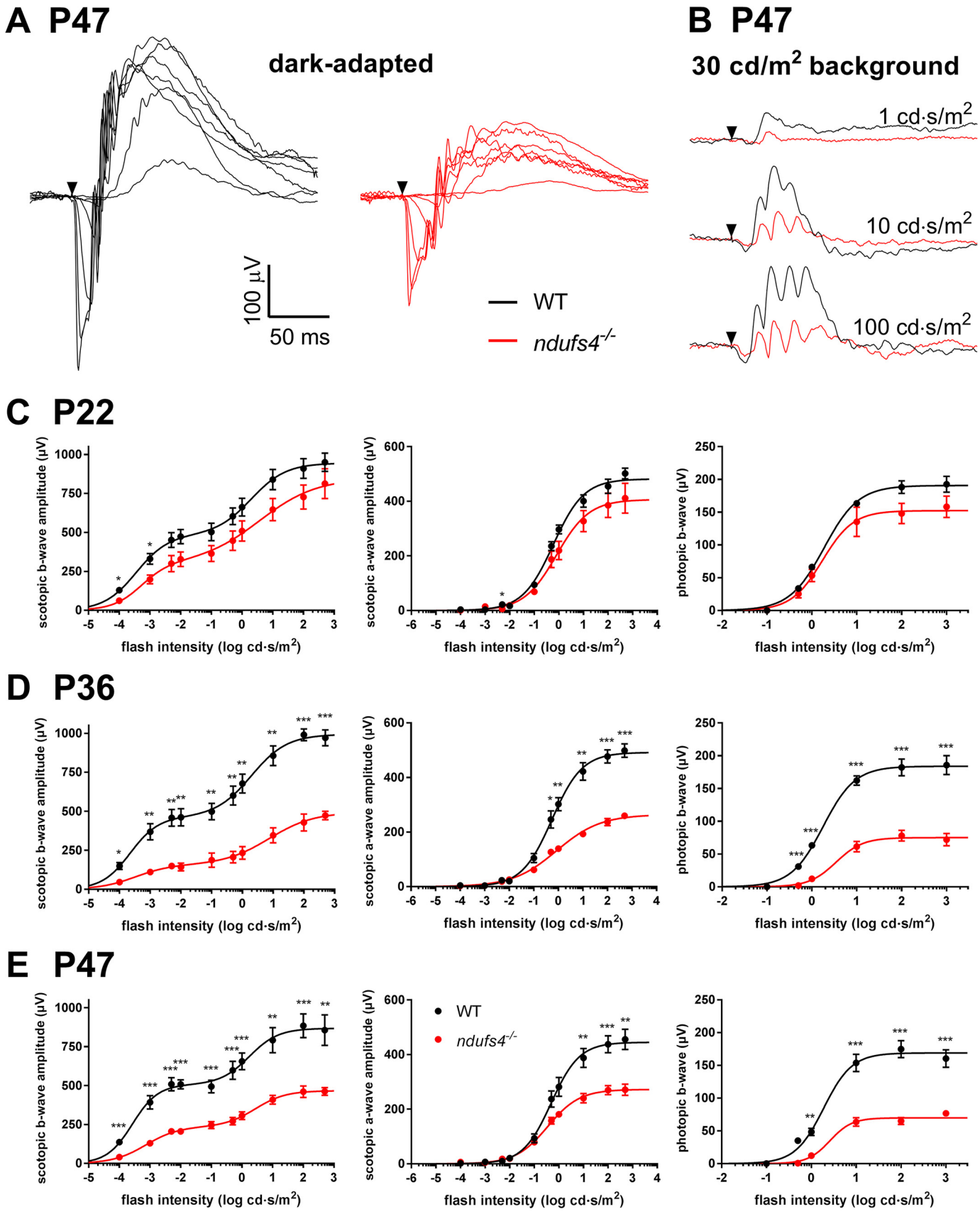
A P47
dark-adapted
100 µV
50 ms
WT
ndufs4-/-
B P47
30 cd/m2 background
1 cd·s/m2
10 cd·s/m2
100 cd·s/m2
C P22
D P36
E P47
scotopic b-wave amplitude (µV)
scotopic a-wave amplitude (µV)
photopic b-wave (µV)
flash intensity (log cd·s/m2)

related to pathology within the RPE. The RPE plays important roles in supporting photoreceptors, including delivery of metabolic substrates from the choroidal circulation and regeneration of the 11-*cis*-retinal chromophore. We therefore assessed morphologic signs of RPE pathology by EM. No difference in RPE cell thickness was found, and although the posterior segments of some *ndufs4*$^{-/-}$ eyes demonstrated occasional RPE cells with large cytoplasmic vacuoles (Fig. 4*A*), these were not observed in every mouse, whereas diminished ERG amplitudes were observed in every *ndufs4*$^{-/-}$ mouse studied. No overt differences in RPE mitochondrial morphology or organization of cristae were observed. However, *ndufs4*$^{-/-}$ RPE cells displayed a higher density of mitochondria than WT (1.01 ± 0.06 *versus* 0.65 ± 0.01 mitochondria μm^{-2}, respectively; $p < 0.001$), as observed previously in other cell types of humans (18) and mice (12) with complex I dysfunction.

We next determined whether the ERG abnormalities reflected an overall decrease in photoreceptor responses due to reduced regeneration of 11-*cis*-retinal by RPE by measuring the retinal content of rhodopsin using difference spectroscopy. However, in concordance with our Western blot analysis (Fig. 2*C*), no difference in rhodopsin content was noted between P47 *ndufs4*$^{-/-}$ and WT retinas after 6 h of dark adaptation, the same duration of dark adaptation given to animals prior to ERG testing ($p = 0.21$; Fig. 4*B*).

The ERG defect in ndufs4$^{-/-}$ *mice can be rescued by modulating the extracellular environment*

The lack of any overt pathology in *ndufs4*$^{-/-}$ photoreceptors may suggest that ERG defects observed in these mice derive from insufficient energy production within photoreceptors or from dysfunction of neighboring cell types adversely affecting their extracellular environment. One possibility, previously described for MCT-3 lactate transporter– deficient mice (19), is decreased uptake of photoreceptor-derived lactic acid by the RPE. We explored this hypothesis by measuring the lactate content in isotonic washes of freshly dissected retinas. However, we observed no difference in the amount of lactate recovered from *ndufs4*$^{-/-}$ retinas compared with WT controls after washes of 2 ($p = 0.32$) or 10 min ($p = 0.83$) (Fig. 4*C*), suggesting that pathological acidification of the interphotoreceptor matrix from accumulation of lactic acid was unlikely to occur in the mutant mice.

To further explore the role of the extracellular environment in the ERG phenotype of *ndufs4*$^{-/-}$ mice, we performed *ex vivo* ERG recordings from isolated P41 retinas equilibrated in Ames' medium. Both retinas from five male *ndufs4*$^{-/-}$ mice and four male WT mice were recorded. To examine whether the deletion of NDUFS4 affects the rod phototransduction cascade, we recorded families of transretinal responses to test flashes of increasing light intensities (Fig. 5). The presence of postsynaptic inhibitors in the perfusion solution blocked contributions of higher-order response components (such as ERG b-waves driven by ON-bipolar cells), allowing isolation of the pure rod photoresponse (20).

Strikingly, in contrast to the ERG results obtained *in vivo*, retinas of dark-adapted control and NDUFS4-deficient mice produced rod light responses of comparable amplitudes (Fig. 5, *A* and *B*). The dim-flash response kinetics for *ndufs4*$^{-/-}$ and control rods were also comparable, with average time-to-peak values of 128 and 130 ms, respectively. The activation kinetics of rod phototransduction, measured from the rising phase of the dim-flash response, was unaffected by NDUFS4 deletion (Fig. 5*C*). The initial phase of response inactivation was also unaltered in *ndufs4*$^{-/-}$ rods, whereas the very late phase of the recovery revealed a slight acceleration. Surprisingly, the recovery following saturating flashes was moderately slower in the mutant mice, as evident from the average kinetics of maximal rod responses (Fig. 5*D*). The molecular mechanisms for these subtle changes in kinetics are unclear, although they might be related to small, long-term compensatory changes in expression and/or function of phototransduction proteins due to the altered metabolic state of the retina. Notably, the average rod photosensitivity (defined as a half-saturating light intensity ($I_{0.5}$)) in mutant mice was not statistically significantly different from that in WT animals (23 ± 3 *versus* 29 ± 5 photons μm^{-2}, respectively; $p > 0.05$) (Fig. 5, *E* and *F*).

Taken together, these results indicate that the lack of the NDUFS4 subunit in mouse rods impairs their signaling *in vivo* but not *ex vivo*. Thus, the intrinsic capacity of mutant photoreceptors to respond to light is preserved and can be restored under *ex vivo* conditions when the retinal tissue is supplemented with proper nutrients to maintain its function. This further suggests that mutant photoreceptors do not undergo major irreversible changes. Rather, the energy deprivation in the outer retina either restricts their energy supply or modifies the molecular or ionic composition of the interphotoreceptor matrix, such that rods and cones cannot operate at their normal capacity.

Discussion

Our electrophysiological characterization of *ndufs4*$^{-/-}$ mice *in vivo* has confirmed the presence of abnormal retinal signaling and further revealed that ERG a- and b-waves are proportionally diminished in these mice, implicating photoreceptors as the primary origin of this visual impairment. Our data suggest that this phenomenon cannot be explained by an irreversible process, such as aberrant photoreceptor development or photoreceptor degeneration. Instead, *ndufs4*$^{-/-}$ photoreceptor function can be completely restored by bathing isolated retinas in standardized recording media, suggesting that photoreceptors with diminished capacity for oxidative metabolism are

Figure 1. Reduced rod and cone light responses in *ndufs4*$^{-/-}$ mice *in vivo*. *A*, representative traces from ERG recordings of dark-adapted WT and *ndufs4*$^{-/-}$ mice at P47 with stimulus intensities ranging from 0.0001 to 500 cd·s/m^2. *Black arrowhead* denotes the application of the light stimulus. *B*, representative photopic light responses in P47 WT and *ndufs4*$^{-/-}$ mice, recorded at the three indicated stimulus intensities. *C–E*, ERG responses of dark-adapted WT and *ndufs4*$^{-/-}$ mice at P22, P36, and P47 are plotted as a function of flash intensity and fit using a double- or single-hyperbolic function. The *left panels* show scotopic b-wave amplitudes, *middle panels* show scotopic a-wave amplitudes, and *right panels* show photopic b-wave amplitudes. Four eyes were analyzed for each genotype at P22 and P36, and six eyes were analyzed per genotype at P47; *Error bars* represent S.E. Results of two-tailed *t* tests between responses from WT and *ndufs4*$^{-/-}$ mice at each flash intensity are presented as follows: *, $p < 0.05$; **, $p < 0.01$; ***, $p < 0.001$. See Table 1 for fitting parameters.

Table 1

Fitting parameters for in vivo ERG recordings and statistical analysis of the differences among selected groups

R_{max}, maximal response amplitude (μV); $I_{0.5}$, half-saturating light intensity (cds/m^2); n, Hill coefficient. Four eyes of two mice of each genotype were recorded for P22 and P36, and six eyes of three mice of each genotype were recorded at P47. p values were calculated to determine the statistical significance between the curve fits for each genotype using an F test. KO, knockout.

		Scotopic b-wave						Scotopic a-wave					Photopic b-wave			
		$R_{max,1}$	$I_{0.5,1}$	n_1	$R_{max,2}$	$I_{0.5,2}$	n_2	R^2	p value	R_{max}	$I_{0.5}$	n	R^2	p value	R_{max}	$I_{0.5}$	n	R^2	p value
P22																			
	WT	484 ± 86	0.0004 ± 0.0003	0.8 ± 0.4	461 ± 113	2.0 ± 1.5	0.8 ± 0.4	0.8842	<0.0001	482 ± 12	0.59 ± 0.09	0.7 ± 0.07	0.9767	<0.0001	191 ± 5	1.9 ± 0.3	1.1 ± 0.1	0.9743	0.0005
	KO	299 ± 184	0.0005 ± 0.0007	0.9 ± 0.9	550 ± 320	3.7 ± 5.7	0.5 ± 0.4	0.8185		406 ± 25	0.80 ± 0.29	0.7 ± 0.14	0.9003		152 ± 9	1.7 ± 0.5	1.3 ± 0.4	0.9026	
P36																			
	WT	463 ± 68	0.0002 ± 0.0001	0.9 ± 0.5	531 ± 99	2.0 ± 1.2	0.7 ± 0.3	0.8888	<0.0001	492 ± 15	0.55 ± 0.10	0.7 ± 0.08	0.9667	<0.0001	184 ± 6	1.8 ± 0.3	1.2 ± 0.2	0.9623	<0.0001
	KO	156 ± 69	0.0003 ± 0.0005	0.8 ± 0.8	339 ± 125	7.5 ± 7.6	0.6 ± 0.4	0.8764		264 ± 8	0.86 ± 0.17	0.5 ± 0.04	0.9866		75 ± 4	3.5 ± 1.1	1.4 ± 0.3	0.9045	
P47																			
	WT	506 ± 55	0.0003 ± 0.0001	1.0 ± 0.4	362 ± 84	1.7 ± 1.3	0.9 ± 0.6	0.7588	<0.0001	445 ± 18	0.49 ± 0.11	0.8 ± 0.12	0.8923	<0.0001	169 ± 8	1.9 ± 0.5	1.4 ± 0.4	0.8788	<0.0001
	KO	236 ± 39	0.0007 ± 0.0004	0.8 ± 0.3	231 ± 50	2.8 ± 1.8	0.9 ± 0.4	0.8684		272 ± 8	0.35 ± 0.07	0.7 ± 0.08	0.9432		70 ± 3	2.6 ± 0.7	1.8 ± 0.4	0.9306	

nevertheless intrinsically capable of accomplishing essentially normal phototransduction.

There is precedence for mice with morphologically normal photoreceptors producing abnormal ERG responses *in vivo*. Examples of such observations include mice with deletions of MCT-3 (19), phospholipase C β4 (21), and carbonic anhydrase XIV (22). Notably, the first two cases also demonstrated normal *ex vivo* light-evoked electrical responses (suction electrode recordings of isolated rods in both cases), whereas the carbonic anhydrase–knockout mouse was not further characterized in this context. None of these mouse lines suffers from a severe systemic phenotype, in contrast to the *ndufs4*$^{-/-}$ mice used in the present study, and they continue to demonstrate normal photoreceptor morphology well into adulthood. In the cases of MCT-3 and carbonic anhydrase XIV, neither protein is expressed by photoreceptors but instead by RPE (MCT-3) and/or Müller glia (both proteins). Loss of MCT-3 results in accumulation of extracellular retinal lactate (19), likely due to the inability of excess lactate to traverse the basolateral membrane of the RPE into the choroidal circulation. Although not directly tested, reduced efflux of lactic acid would be predicted to result in acidification of the interphotoreceptor matrix. Similarly, carbonic anhydrase has been shown to buffer the pH of the interphotoreceptor matrix, with its inhibition resulting in acidification of this compartment (23). Interphotoreceptor matrix acidification might explain the abnormal *in vivo* ERG responses in both mutations, as low pH is known to decrease the activity of the rod outer segment $Na^+/Ca^{2+}/K^+$ exchanger NCKX1 (24), which maintains Ca^{2+} homeostasis in the outer segment and is critical in supporting normal rod sensitivity and response amplitude (25). The mechanism behind reduced ERG amplitudes in phospholipase C β4–knockout retinas is less clear but may also be related to altered Ca^{2+} homeostasis.

In this context, what could explain why *ndufs4*$^{-/-}$ photoreceptors produce diminished light responses *in vivo* but normal responses *ex vivo*? One possibility is that the mutant photoreceptors themselves are incapable of generating enough energy to support electrochemical gradients of ions involved in producing electrical light responses. This could be compensated in the recording medium by 1) providing photoreceptors with an essentially unlimited supply of glucose and 2) providing constant extracellular ion conditions, thereby reducing the burden of establishing ion gradients across the cell membrane. Indeed, an emerging understanding of metabolic flux within vertebrate retinas indicates that photoreceptors rely on aerobic glycolysis rather than OX-PHOS as their primary energy source (26, 27), suggesting that an unlimited glucose supply may compensate for reduced mitochondrial function.

Another, not mutually exclusive, possibility is that abnormal energy metabolism within other neighboring cell types contributes to *in vivo* pathology. One plausible hypothesis is related to the role of the RPE in supporting the flux of glucose and lactate between the choroid and the retina. RPE cells serve as a conduit for glucose entry to the retina by expressing the facilitative glucose transporter GLUT1 at both the basolateral and apical membranes (28) and for efflux of retinal lactate by expressing the facilitative lactate transporters MCT-1 and MCT-3 on the apical and basolateral membranes, respectively (29). Impor-

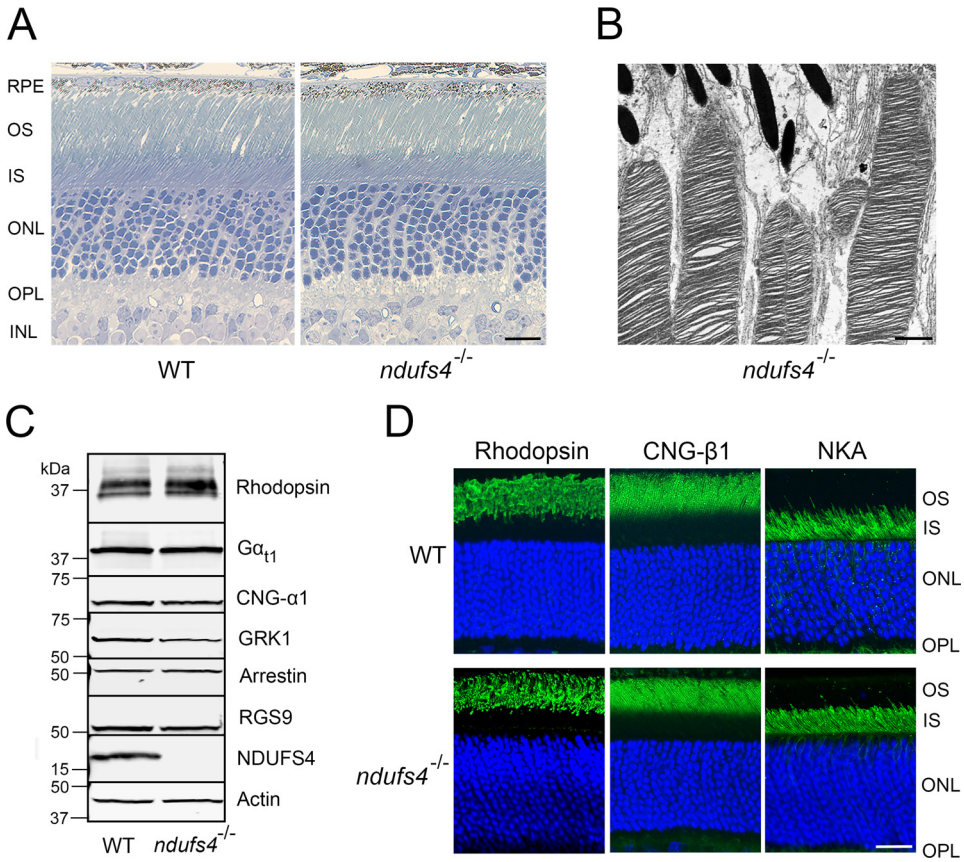

Figure 2. Normal photoreceptor morphology in *ndufs4*$^{-/-}$ mice. *A*, plastic cross-sections of WT (*left*) and *ndufs4*$^{-/-}$ (*right*) retinas at P47. *Scale bar*, 10 μm. *OS*, outer segments; *IS*, inner segments; *ONL*, outer nuclear layer; *OPL*, outer plexiform layer; *INL*, inner nuclear layer. *B*, electron micrograph of distal outer segments of photoreceptors from a P47 *ndufs4*$^{-/-}$ retina. *Scale bar*, 1 μm. *C*, Western blot analysis of retinal lysates (25 μg loaded per lane) determining expression levels of NDUFS4 protein and of representative proteins relevant to phototransduction in WT and *ndufs4*$^{-/-}$ retinas. Actin is the loading control. $G\alpha_{t1}$, rod transducin; *GRK1*, rhodopsin kinase; *RGS9*, regulator of G-protein signaling member 9. *D*, immunolocalization of rhodopsin, CNG-β1, and the Na^+/K^+-ATPase (*NKA*) within rod photoreceptors. *Scale bar*, 20 μm.

tantly, in addition to providing a route for retinal lactate to exit into the choroidal circulation, RPE cells also have a high capacity to use photoreceptor-derived lactate as a substrate for oxidative metabolism (26). In fact, metabolizing lactate allows the RPE to spare glucose passing from the choroid to the interphotoreceptor matrix (26). Once there, the glucose can then be taken up by photoreceptors via GLUT1 in the inner segments (30). Impaired OX-PHOS within the *ndufs4*$^{-/-}$ RPE could lead to a reduced ability to metabolize lactate and a greater reliance on glycolysis, thereby limiting glucose delivery to photoreceptors. Bathing the *ndufs4*$^{-/-}$ retinas in recording media eliminates their reliance on RPE for glucose supply, thus potentially explaining the restoration of normal photoreceptor signaling *ex vivo*. Testing this hypothesis would require generation of transgenic mice with cell-specific deletion of *ndufs4* in photoreceptors or RPE to determine which cell type is primarily responsible for the *in vivo* ERG phenotype.

It is instructive to compare our results with those addressing the retinal phenotype of the *agc1*/*aralar*-knockout mouse also suffering from impaired OX-PHOS (31). AGC1/Aralar is the neuronal isoform of the mitochondrial aspartate–glutamate carrier, and its absence makes affected cells unable to efficiently regenerate NAD^+ via oxidative metabolism due to impairment of the malate–aspartate shuttle on the mitochondrial membrane (32). Because cytosolic NAD^+ is required for additional rounds of glycolysis, pyruvate must be reduced to lactate in the cytosol of these cells to regenerate NAD^+, rather than entering mitochondria as a substrate for the Krebs cycle. Similar to *ndufs4*$^{-/-}$ mice, *agc1*/*aralar*-knockout mice develop both systemic (32) and retinal (31) phenotypes. These mice also display a marked ~40–50% reduction in a- and b-wave ERG amplitudes recorded from dark-adapted animals despite no evidence of retinal morphologic abnormalities. Their ERG responses were partially improved after brief exposure to background illumination. Because light adaptation is thought to reduce the metabolic demand of photoreceptors (33), this result suggests that the mutant photoreceptors function at the limit of their metabolic capacity. It would be interesting to determine whether the *agc1*/*aralar*-knockout mouse exhibits restoration of normal signaling in isolated retinas and whether this gene is expressed in both photoreceptors and RPE.

Finally, with regard to the applicability of our findings to human patients, there is scant literature available on ERG assessments of outer retinal function in patients with Leigh syndrome and LHON. Given that pigmentary retinopathy is known to develop in some patients with Leigh syndrome, abnormal ERG responses consistent with retinal dystrophy would be expected, and one study reported this finding in 23% of children with Leigh syndrome (10). However, the patients in this report had mutations in genes other than *ndufs4*, so the

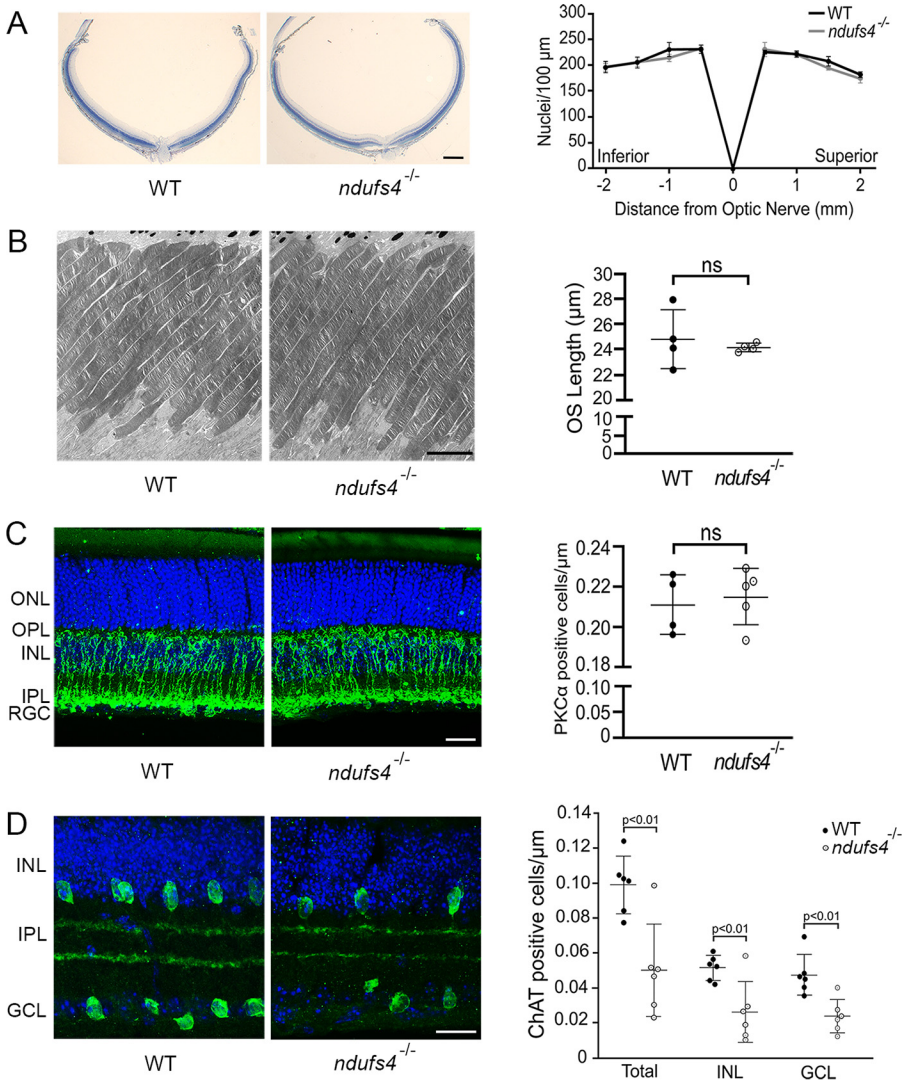

Figure 3. Histologic analysis of *ndufs4*$^{-/-}$ retinas. *A*, representative retinal cross-sections of WT and *ndufs4*$^{-/-}$ retinas at P47, oriented with the inferior pole to the *left* and superior pole to the *right*. *Scale bar*, 200 μm. To the *right*, a spider diagram depicts outer nuclear layer density (nuclei per 100 $\times$ 100-μm box) at specified distances from the optic nerve head. *Error bars* represent S.E. $n = 4$ retinas per genotype. *B*, electron micrographs of WT and *ndufs4*$^{-/-}$ photoreceptor outer segments at P47. *Scale bar*, 5 μm. The scatter plot to the *right* compares outer segment length ($n = 4$ retinas per genotype; 25 outer segments measured per retina; *bars* depict mean $\pm$ S.D.). *C* and *D*, immunolabeling of rod bipolar cells with PKC-α (*C*) and of starburst amacrine cells with ChAT (*D*) in P49 WT and *ndufs4*$^{-/-}$ retinal cross-sections. *Scale bar,* 20 (*C*) and 10 μm (*D*). Scatter plots to the *right* compare cell density (labeled cells per μm of nuclei in the respective nuclear layers). $n = 5$ WT and 4 *ndufs4*$^{-/-}$ retinas for PKC-α; $n = 6$ WT and 6 *ndufs4*$^{-/-}$ retinas for ChAT. *Bars* indicate mean $\pm$ S.D. *ns*, not significant. *OS*, outer segments; *IS*, inner segments; *ONL*, outer nuclear layer; *OPL*, outer plexiform layer; *INL*, inner nuclear layer; *IPL*, inner plexiform layer; GCL, ganglion cell layer.

prevalence of ERG abnormalities in this particular genotype remains to be determined. Among rare reports of outer retinal functional assessments in LHON, an asymptomatic mother carrying the 11778 mtDNA mutation in the ND4 complex I subunit and her affected adolescent son both demonstrated full-field ERG abnormalities suggestive of cone dysfunction (34). Another study reported one of two patients with the 11778 mutation demonstrating an abnormal ERG suggestive of rod–cone dystrophy (35). A separate report on an extensive Brazilian pedigree of the 11778 mutation reported that multifocal ERG abnormalities were commonly noted among asymptomatic carriers, although it was not specified whether this reflected photoreceptor dysfunction in addition to inner retinal pathology (36). It would be important to gain further insight into the degree of visual impairment in these patients, such as decreased ability to see under dim-light conditions and to recognize low-contrast objects.

Experimental procedures

Animals

Mice heterozygous for a deletion of exon 2 of *ndufs4* on a C57BL/6 genetic background (13) were purchased from The Jackson Laboratory (stock number 027058) and were free of RD1 and RD8 mutations. Heterozygous mice were crossed to generate homozygous *ndufs4*$^{-/-}$ animals and WT littermates as controls. Animals were reared under a normal day/night cycle and handled according to a protocol approved by the Institutional Animal Care and Use Committee of Duke University. All experiments were performed during the day.

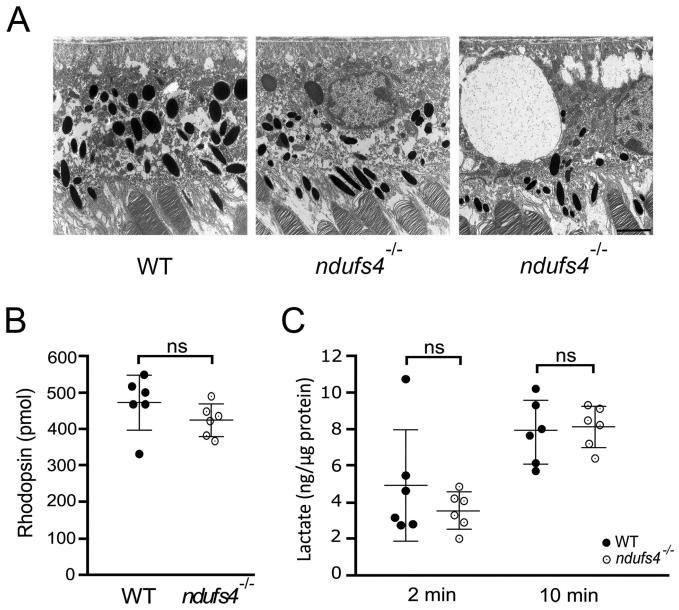

Figure 4. Retinal pigment epithelium morphology and function in *ndufs4*$^{-/-}$ mice. *A*, electron micrographs of RPE cells at P47. Although most *ndufs4*$^{-/-}$ RPE (*middle panel*) had a morphology similar to WT (*left*), occasional *ndufs4*$^{-/-}$ RPE cells (*right*) were observed to have giant intracellular vacuoles. *Scale bar*, 2 μm. *B*, rhodopsin content of isolated WT and *ndufs4*$^{-/-}$ retinas at P47, as measured by difference spectroscopy. $n = 6$ retinas per genotype. *C*, quantification of lactate liberated from isotonic washes of isolated retinas. In separate experiments, WT and *ndufs4*$^{-/-}$ retinas were washed for 2 or 10 min, and the lactate content was normalized to total retinal protein for each sample. $n = 6$ retinas per genotype in each experiment. *Bars* indicate mean ± S.D. *ns*, not significant.

Antibodies

The following antibodies were used for immunofluorescence experiments: mouse monoclonal 4D2 against rhodopsin (1:100; Abcam, ab98887), rabbit polyclonal anti-cyclic nucleotide-gated cation channel (CNG)-β1 (1:200; a gift from Steven Pittler, University of Alabama, Birmingham, AL), mouse monoclonal anti-Na^+/K^+-ATPase (1:500; Santa Cruz Biotechnology, sc-58628, lot number I2413), mouse anti-PKC-α H-7 (1:100; Santa Cruz Biotechnology, sc-8393, lot number I1306), and goat polyclonal anti-choline acetyltransferase (1:100; Millipore, AB144P, lot number 3169862). The following antibodies were used for Western blot analysis of retinal lysates: mouse monoclonal anti-NDUFS4 1-E-4 (1:200; Santa Cruz Biotechnology, sc-100567, lot number A2918), mouse monoclonal anti-β-actin (1:1000; Santa Cruz Biotechnology, sc-47778, lot number D0615), mouse monoclonal 4D2 (1:5000), rabbit polyclonal anti-rod transducin-α, $G_{\alpha t1}$ K-20 (1:500; Santa Cruz Biotechnology, sc-389, lot number C0916), mouse monoclonal anti-arrestin C10C10 (1:1000; Ref. 37), goat polyclonal anti-CNG-α T-18 (1:500; Santa Cruz Biotechnology, sc-13694, lot number K1208), goat polyclonal anti-regulator of G-protein signaling member 9 (RGS9) T-19 (1:500; Santa Cruz Biotechnology, sc-8143, lot number L1205), and mouse monoclonal anti-rhodopsin kinase (GRK1) G-8 (1:500; Santa Cruz Biotechnology, sc-8004, lot number A289). Secondary antibodies against the appropriate species conjugated to Alexa Fluor 488 (immunofluorescence experiments; 1:500 dilution) or Alexa Fluor 680 (Western blotting experiments; 1:20,000 dilution) were purchased from Invitrogen. Cell nuclei were stained using 4′,6-diamidino-2-phenylindole (DAPI) (Sigma-Aldrich).

Electroretinography

ERGs were recorded in live mice of both sexes as described previously (15, 38) using the Espion E2 system with a Color-Dome Ganzfeld stimulator (Diagnosys LLC, Littleton, MA). Briefly, after dark adaptation for 6 h, mice were anesthetized by an intraperitoneal injection of 90 mg/kg ketamine and 9 mg/kg xylazine. Pupils were dilated with a mixture of 1% cyclopentolate HCl and 2.5% phenylephrine. Lubrication of the eyes during the recordings was maintained by a 1% carboxymethylcellulose sodium gel, and body temperature was maintained by a heated platform. Simultaneous recordings were made from both eyes using gold contact lens electrodes (Mayo Corp., Oasuka, Japan) with stainless steel needle electrodes (Ocuscience) in the mouth (reference) and at the base of the tail (ground). ERG signals were sampled at 1 kHz and recorded with 0.15-Hz low-frequency and 500-Hz high-frequency cutoffs. Responses to flashes from 0.0001 to 500 cd·s/m^2 with 1–10 trials (fewer trials for the brighter stimuli) averaged and interflash intervals of 5–180 s were recorded in the dark, and then flashes from 0.1 to 1000 cd·s/m^2 were recorded in the presence of rod-saturating light of 30 cd/m^2. Following the recordings, the mice were euthanized for histological analysis.

The data from the ERG recordings were analyzed using MATLAB 2016a (MathWorks). Oscillatory potentials were removed from the signals by 55-Hz fast Fourier transform low-pass frequency filtering. The amplitude of the b-wave was calculated from baseline to the peak for dimmer flashes and from the bottom of the a-wave to the b-wave peak for brighter flashes. Data points from the a-wave and b-wave stimulus–response curves were fitted by single (Equation 1)- or double-hyperbolic functions (Equation 2), respectively, using the least-square fitting procedure. R is the transient-peak amplitude of the rod response, R_{max} is the maximal response amplitude, I is the flash intensity, n is the Hill coefficient (exponent), and $I_{0.5}$ is the half-saturating light intensity. p values were calculated to determine the statistical significance between the curve fits in each condition using an F test and between the response amplitudes of *ndufs4*$^{-/-}$ and WT mice at each flash intensity using two-tailed t tests in GraphPad software.

$$R = R_{max}\frac{I^n}{I^n + I_{0.5}^n} \quad \text{(Eq. 1)}$$

$$R = R_{max,1}\frac{I^{n_1}}{I^{n_1} + I_{0.5,1}^{n_1}} + R_{max,2}\frac{I^{n_2}}{I^{n_2} + I_{0.5,2}^{n_2}} \quad \text{(Eq. 2)}$$

Ex vivo ERG recordings were performed on isolated mouse retinas. After dark adaptation overnight, mice were sacrificed by CO_2 asphyxiation. Each retina was removed from its eyecup under IR illumination and stored in oxygenated Ames' medium (Sigma-Aldrich) at room temperature. The retina was mounted on filter paper with the photoreceptor side up and placed in a perfusion chamber (39) between two electrodes connected to a differential amplifier. The sample was perfused with bicarbon-

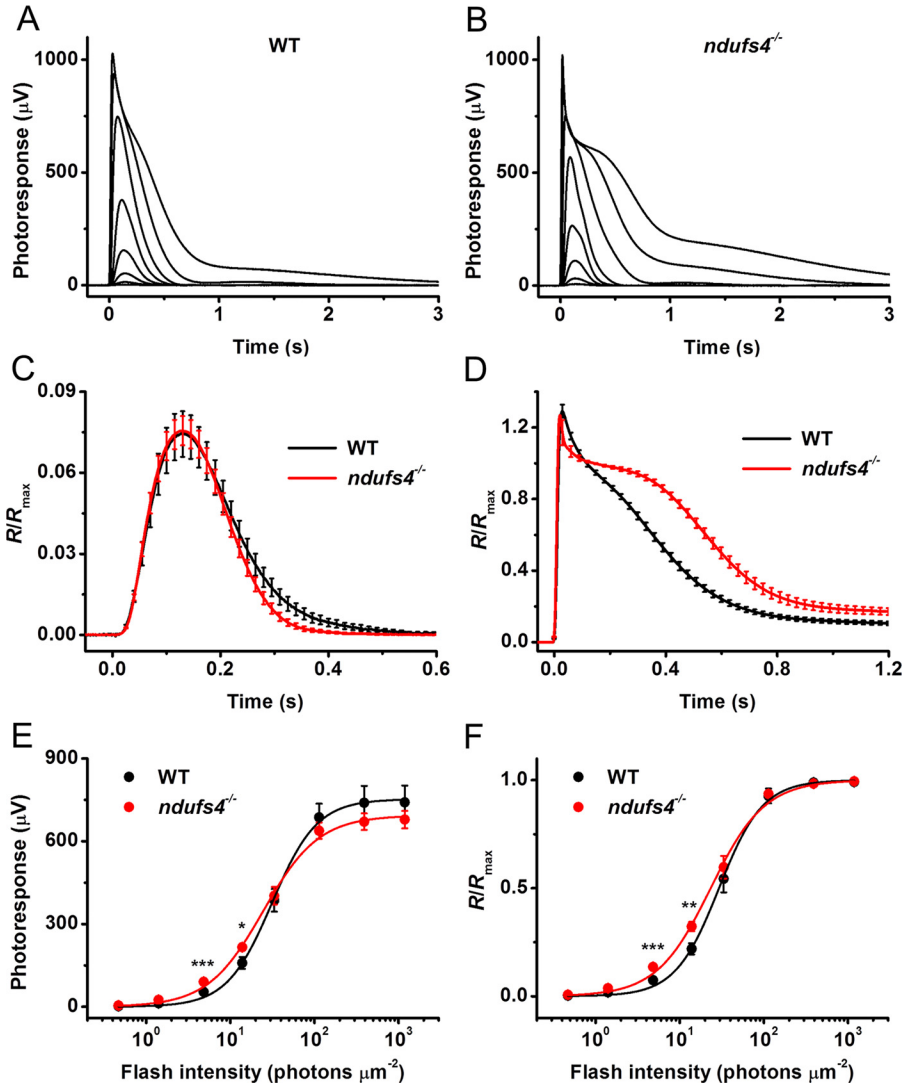

Figure 5. Normal rod light responses in isolated *ndufs4*$^{-/-}$ retinas. *A*, representative family of rod responses from isolated WT mouse retina. Test flashes of 505-nm light with intensities of 0.5, 1.4, 4.8, 14, 33, 114, 392, and 1188 photons μm^{-2} were delivered at time 0. *B*, representative family of rod responses from isolated *ndufs4*$^{-/-}$ mouse retina. Test flashes of 505-nm light had the same intensities as in *A*. *C*, kinetics of rod phototransduction activation and inactivation in control and *ndufs4*$^{-/-}$ mice. Population-averaged dim-flash responses to test stimuli of 4.8 photons μm^{-2} ($n = 8$ for controls and $n = 10$ for mutants) were normalized to R_{max} of respective retinas. *D*, comparison of saturated rod responses from WT and *ndufs4*$^{-/-}$ mice. Population-averaged responses to test stimuli of 1188 photons μm^{-2} ($n = 8$ for controls and $n = 10$ for mutants) were normalized to R_{max} of respective retinas. *E*, averaged rod intensity–response functions for WT ($n = 8$) and *ndufs4*$^{-/-}$ ($n = 10$) retinas. Points were fitted with hyperbolic Naka–Rushton functions as described under "Experimental procedures." *F*, normalized averaged rod intensity–response relationships for control ($n = 8$) and *ndufs4*$^{-/-}$ ($n = 10$) retinas. Naka–Rushton fits yielded $I_{0.5}$ values of 29 and 23 photons μm^{-2} for WT and *ndufs4*$^{-/-}$ mice, respectively. The statistical significance of the data in *E* and *F* is represented as follows: *, $p < 0.05$; **, $p < 0.01$; ***, $p < 0.001$. All recordings were from P41 control and *ndufs4*$^{-/-}$ mice. *Error bars* represent S.E. in all panels.

ate-buffered Ames' medium (Sigma-Aldrich) supplemented with 40 μM DL-2-amino-4-phosphonobutyric acid to block postsynaptic components of the photoresponse (40) and with 100 μM $BaCl_2$ to suppress the slow glial PIII component (41). The perfusion solution was continuously bubbled with a 95% O_2, 5% CO_2 mixture, and its temperature was maintained at 36–37 °C with a heater.

The retina was stimulated with 20-ms test flashes of calibrated 505-nm light-emitting diode (LED) light. The light intensity was controlled by neutral density filters and a computer in 0.5 log-unit steps. Intensity–response relationships were fitted with the following Naka–Rushton hyperbolic functions (Equation 3 for raw data and Equation 4 for normalized data).

$$R = \frac{R_{max} \cdot I^n}{I^n + I_{0.5}^n} \quad \text{(Eq. 3)}$$

$$\frac{R}{R_{max}} = \frac{I^n}{I^n + I_{0.5}^n} \quad \text{(Eq. 4)}$$

Photoresponses were amplified by a differential amplifier (DP-311, Warner Instruments), low-pass-filtered at 300 Hz (eight-pole Bessel), and digitized at 1 kHz. Data were analyzed with Clampfit 10.4 and Origin 8.5 software. All data were expressed as mean ± S.E. and analyzed with the independent two-tailed Student's *t* test (using an accepted significance level of $p < 0.05$).

Histological techniques

The eyes of euthanized mice were enucleated, and posterior eyecups were dissected and fixed for 1 h in 4% paraformaldehyde and rinsed in PBS. Agarose-embedded retinal cross-sections were prepared as described (42). 100-μm-thick cross-sections from the central portion of the retina were collected with a vibratome (Leica VT1200S) in 24-well plates, and floating sections were then incubated for 4 h with the blocking solution containing 5% goat serum and 0.03% Triton X-100 in PBS buffer on an orbital shaker. Sections were further incubated overnight with the corresponding primary antibodies, washed three times with PBS, incubated for 2 h with appropriate secondary antibody conjugated to Alexa Fluor 488 (1:500), and washed three times in PBS. Alternatively, retinal cryosections were prepared by cryoprotecting fixed eyecups in 30% sucrose and embedding them in optimal cutting temperature (OCT) medium (Tissue-Tek, Sakura Finetek). Retinal 20-μm cross-sections were collected using a cryostat microtome (Microm HM 550, Thermo Fisher Scientific). Sections were rehydrated with PBS, blocked with 5% goat or donkey serum in PBS with 0.03% Triton X-100 for 1 h, incubated in primary antibody in the same blocking solution overnight, washed three times, incubated in secondary antibodies in blocking solution, and then finally washed three more times. Both agarose sections and cryosections were mounted with Vectashield (Vector Laboratories) under glass coverslips. Images were acquired using a Nikon Eclipse Ti2 inverted confocal microscope, CFI Plan Fluor 20× or 60× (oil) objectives, and an A1 confocal scanner controlled by NIS-Elements software (Nikon). In the case of PKC-α– and choline acetyltransferase (ChAT)-stained cryosections, 45,000-μm^2 images spaced 500 μm on either side of the optic nerve head were obtained on three sections for each retina. The number of positive nuclei/μm of inner nuclear layer or ganglion cell layer was averaged for each retina.

For experiments involving analysis of mouse retinas in plastic sections, the superior limbus of each eye was marked with cautery to facilitate proper orientation prior to enucleation and fixation in 2% glutaraldehyde and 2% paraformaldehyde. 1-μm plastic-embedded cross-sections of the mouse retina were prepared as described (43) and stained with toluidine blue for light microscopy. Nuclear counts in 100-μm segments of the outer nuclear layer were performed in sections cut through the optic nerve at 500-μm steps from the optic nerve head. The same specimens were also processed for transmission EM. Thin sections of 60–80 nm were collected on copper grids, counterstained with uranyl acetate and Sato's lead, and examined using an electron microscope (JEM-1400, JEOL) at 60 kV. Images were collected using a charge-coupled device camera (Orius, Gatan).

Rhodopsin quantification

Rhodopsin concentration was determined by difference spectroscopy using the molar extinction coefficient 40,500 $cm^{-1}\ M^{-1}$ (44, 45). Individual retinas were extracted under dim-red illumination and sonicated in 250 μl of deionized water. A 100-μl aliquot was mixed with 20 μl of 200 mM hydroxylamine, pH 7.5, containing 10% *n*-octyl β-D-glucopyranoside. The sample was centrifuged in a tabletop microcentrifuge, and rhodopsin concentration in the supernatant was determined from the absorbance at 500 nm before and after complete bleaching of the sample.

Retinal washes and extracts for lactate quantification and Western blotting

Measurements of extracellular lactate in WT and *ndufs4*$^{-/-}$ mouse retinas were performed, adapted from a previously described protocol (19). Briefly, dark-adapted mice were euthanized in the light and immediately enucleated. Posterior eyecups were dissected, and each retina was removed using forceps. Retinas were then placed in a microcentrifuge tube containing 50 μl of PBS and incubated for 1 or 9 min. The samples were centrifuged at 14,000 × *g* for 1 min, and the supernatant was removed for a lactate assay, performed in duplicates using a colorimetric lactate assay (Cell Bio-Labs). The pelleted retinas were then solubilized in 100 μl of lysis buffer (25 mM HEPES buffer, pH 7.4, 150 mM NaCl, 5 mM $MgCl_2$, and protease inhibitors (Complete Mini, Roche Applied Science) containing 1% Triton X-100), and the protein concentration of each lysate was determined with a colorimetric assay (Bio-Rad). The lactate concentration in the retinal wash was normalized to detergent-soluble protein concentration for each retina.

The detergent-soluble retinal lysates were used for Western blot analysis. After mixing with SDS-PAGE sample buffer, retinal lysates from WT and *ndufs4*$^{-/-}$ mice were separated on 4–20% SDS-PAGE gels (25 μg of protein per lane), transferred onto polyvinylidene fluoride (PVDF) membranes and blotted with the indicated primary and secondary antibodies. The blots were imaged using an Odyssey imaging system (LI-COR Biosciences).

Experimental design and statistical analysis

All histological experiments and the *in vivo* electrophysiological experiments were performed on *ndufs4*$^{-/-}$ mice and littermate controls with both sexes represented. The *in vivo* ERG recordings were performed at P22 (four eyes of two *ndufs4*$^{-/-}$ mice and four eyes of two WT mice), at P36 (four eyes of two *ndufs4*$^{-/-}$ mice and four eyes of two WT mice), and P47 (six eyes of three *ndufs4*$^{-/-}$ mice and six eyes of three WT mice). In the case of *ex vivo* ERGs, all recordings were performed on retinas from P41 male *ndufs4*$^{-/-}$ mice (10 retinas from five mice) and age-matched male C57BL/6 controls (eight retinas from four mice). Male mice were selected for this experiment because of the more severe visual dysfunction often seen in male human patients with complex I dysfunction.

To compare sensitivities of different experimental groups, a-wave and b-wave amplitudes recorded at each flash intensity were compared using a two-tailed *t* test in GraphPad Prism version 7.00 for Windows (GraphPad Software). No statistical methods were used to predetermine sample sizes, but sample sizes are similar to those used in previously published studies. No randomization was used, and animal genotypes were not masked.

Author contributions—S. M. G. conceptualization; S. M. G., A. M. T., A. V. K., L. W., V. J. K., and V. Y. A. formal analysis; S. M. G. and V. Y. A. funding acquisition; S. M. G., A. M. T., A. V. K., M. K., and L. W. investigation; S. M. G., A. M. T., A. V. K., V. J. K., and V. Y. A. writing-original draft; S. M. G., A. M. T., A. V. K., M. K., V. J. K., and V. Y. A. writing-review and editing.

Acknowledgment—We thank Ying Hao for technical assistance with histological processing of samples and EM imaging.

References

1. Chacinska, A., Koehler, C. M., Milenkovic, D., Lithgow, T., and Pfanner, N. (2009) Importing mitochondrial proteins: machineries and mechanisms. *Cell* **138,** 628–644 CrossRef Medline
2. Wallace, D. C. (2011) Bioenergetic origins of complexity and disease. *Cold Spring Harb. Symp. Quant. Biol.* **76,** 1–16 CrossRef Medline
3. Sadun, A. A. (2002) Metabolic optic neuropathies. *Semin. Ophthalmol.* **17,** 29–32 CrossRef Medline
4. Lefevere, E., Toft-Kehler, A. K., Vohra, R., Kolko, M., Moons, L., and Van Hove, I. (2017) Mitochondrial dysfunction underlying outer retinal diseases. *Mitochondrion* **36,** 66–76 CrossRef Medline
5. Fraser, J. A., Biousse, V., and Newman, N. J. (2010) The neuro-ophthalmology of mitochondrial disease. *Surv. Ophthalmol.* **55,** 299–334 CrossRef Medline
6. Chinnery, P. F., Johnson, M. A., Wardell, T. M., Singh-Kler, R., Hayes, C., Brown, D. T., Taylor, R. W., Bindoff, L. A., and Turnbull, D. M. (2000) The epidemiology of pathogenic mitochondrial DNA mutations. *Ann. Neurol.* **48,** 188–193 CrossRef Medline
7. Brown, M. D., Trounce, I. A., Jun, A. S., Allen, J. C., and Wallace, D. C. (2000) Functional analysis of lymphoblast and cybrid mitochondria containing the 3460, 11778, or 14484 Leber's hereditary optic neuropathy mitochondrial DNA mutation. *J. Biol. Chem.* **275,** 39831–39836 CrossRef Medline
8. Kirches, E. (2011) LHON: mitochondrial mutations and more. *Curr. Genomics* **12,** 44–54 CrossRef Medline
9. Lake, N. J., Compton, A. G., Rahman, S., and Thorburn, D. R. (2016) Leigh syndrome: one disorder, more than 75 monogenic causes. *Ann. Neurol.* **79,** 190–203 CrossRef Medline
10. Åkebrand, R., Andersson, S., Seyedi Honarvar, A. K., Sofou, K., Darin, N., Tulinius, M., and Grönlund, M. A. (2016) Ophthalmological characteristics in children with Leigh syndrome—a long-term follow-up. *Acta Ophthalmol.* **94,** 609–617 CrossRef Medline
11. Ma, Y. Y., Wu, T. F., Liu, Y. P., Wang, Q., Song, J. Q., Li, X. Y., Shi, X. Y., Zhang, W. N., Zhao, M., Hu, L. Y., Yang, Y. L., and Zou, L. P. (2013) Genetic and biochemical findings in Chinese children with Leigh syndrome. *J. Clin. Neurosci.* **20,** 1591–1594 CrossRef Medline
12. Lin, C. S., Sharpley, M. S., Fan, W., Waymire, K. G., Sadun, A. A., Carelli, V., Ross-Cisneros, F. N., Baciu, P., Sung, E., McManus, M. J., Pan, B. X., Gil, D. W., Macgregor, G. R., and Wallace, D. C. (2012) Mouse mtDNA mutant model of Leber hereditary optic neuropathy. *Proc. Natl. Acad. Sci. U.S.A.* **109,** 20065–20070 CrossRef Medline
13. Kruse, S. E., Watt, W. C., Marcinek, D. J., Kapur, R. P., Schenkman, K. A., and Palmiter, R. D. (2008) Mice with mitochondrial complex I deficiency develop a fatal encephalomyopathy. *Cell Metab.* **7,** 312–320 CrossRef Medline
14. Yu, A. K., Song, L., Murray, K. D., van der List, D., Sun, C., Shen, Y., Xia, Z., and Cortopassi, G. A. (2015) Mitochondrial complex I deficiency leads to inflammation and retinal ganglion cell death in the Ndufs4 mouse. *Hum. Mol. Genet.* **24,** 2848–2860 CrossRef Medline
15. Herrmann, R., Lobanova, E. S., Hammond, T., Kessler, C., Burns, M. E., Frishman, L. J., and Arshavsky, V. Y. (2010) Phosducin regulates transmission at the photoreceptor-to-ON-bipolar cell synapse. *J. Neurosci.* **30,** 3239–3253 CrossRef Medline
16. Song, L., Yu, A., Murray, K., and Cortopassi, G. (2017) Bipolar cell reduction precedes retinal ganglion neuron loss in a complex 1 knockout mouse model. *Brain Res.* **1657,** 232–244 CrossRef Medline
17. Smith, B. J., Côté, P. D., and Tremblay, F. (2017) Contribution of Nav1.8 sodium channels to retinal function. *Neuroscience* **340,** 279–290 CrossRef Medline
18. Korsten, A., de Coo, I. F., Spruijt, L., de Wit, L. E., Smeets, H. J., and Sluiter, W. (2010) Patients with Leber hereditary optic neuropathy fail to compensate impaired oxidative phosphorylation. *Biochim. Biophys. Acta* **1797,** 197–203 CrossRef Medline
19. Daniele, L. L., Sauer, B., Gallagher, S. M., Pugh, E. N., Jr., and Philp, N. J. (2008) Altered visual function in monocarboxylate transporter 3 (Slc16a8) knockout mice. *Am. J. Physiol. Cell Physiol.* **295,** C451–C457 CrossRef Medline
20. Kolesnikov, A. V., and Kefalov, V. J. (2012) Transretinal ERG recordings from mouse retina: rod and cone photoresponses. *J. Vis. Exp.* **61,** 3424 CrossRef Medline
21. Jiang, H., Lyubarsky, A., Dodd, R., Vardi, N., Pugh, E., Baylor, D., Simon, M. I., and Wu, D. (1996) Phospholipase Cβ4 is involved in modulating the visual response in mice. *Proc. Natl. Acad. Sci. U.S.A.* **93,** 14598–14601 CrossRef Medline
22. Ogilvie, J. M., Ohlemiller, K. K., Shah, G. N., Ulmasov, B., Becker, T. A., Waheed, A., Hennig, A. K., Lukasiewicz, P. D., and Sly, W. S. (2007) Carbonic anhydrase XIV deficiency produces a functional defect in the retinal light response. *Proc. Natl. Acad. Sci. U.S.A.* **104,** 8514–8519 CrossRef Medline
23. Borgula, G. A., Karwoski, C. J., and Steinberg, R. H. (1989) Light-evoked changes in extracellular pH in frog retina. *Vision Res.* **29,** 1069–1077 CrossRef Medline
24. Schnetkamp, P. P. (1995) Chelating properties of the Ca^{2+} transport site of the retinal rod Na−Ca+K exchanger: evidence for a common Ca^{2+} and Na^{+} binding site. *Biochemistry* **34,** 7282–7287 CrossRef Medline
25. Vinberg, F., Wang, T., Molday, R. S., Chen, J., and Kefalov, V. J. (2015) A new mouse model for stationary night blindness with mutant Slc24a1 explains the pathophysiology of the associated human disease. *Hum. Mol. Genet.* **24,** 5915–5929 CrossRef Medline
26. Kanow, M. A., Giarmarco, M. M., Jankowski, C. S., Tsantilas, K., Engel, A. L., Du, J., Linton, J. D., Farnsworth, C. C., Sloat, S. R., Rountree, A., Sweet, I. R., Lindsay, K. J., Parker, E. D., Brockerhoff, S. E., Sadilek, M., *et al.* (2017) Biochemical adaptations of the retina and retinal pigment epithelium support a metabolic ecosystem in the vertebrate eye. *Elife* **6,** e28899 CrossRef Medline
27. Chinchore, Y., Begaj, T., Wu, D., Drokhlyansky, E., and Cepko, C. L. (2017) Glycolytic reliance promotes anabolism in photoreceptors. *Elife* **6,** e25946 CrossRef Medline
28. Takata, K., Kasahara, T., Kasahara, M., Ezaki, O., and Hirano, H. (1992) Ultracytochemical localization of the erythrocyte/HepG2-type glucose transporter (GLUT1) in cells of the blood-retinal barrier in the rat. *Invest. Ophthalmol. Vis. Sci.* **33,** 377–383 Medline
29. Philp, N. J., Yoon, H., and Lombardi, L. (2001) Mouse MCT3 gene is expressed preferentially in retinal pigment and choroid plexus epithelia. *Am. J. Physiol. Cell Physiol.* **280,** C1319–C1326 CrossRef Medline
30. Gospe, S. M., 3rd, Baker, S. A., and Arshavsky, V. Y. (2010) Facilitative glucose transporter Glut1 is actively excluded from rod outer segments. *J. Cell Sci.* **123,** 3639–3644 CrossRef Medline
31. Contreras, L., Ramirez, L., Du, J., Hurley, J. B., Satrústegui, J., and de la Villa, P. (2016) Deficient glucose and glutamine metabolism in Aralar/AGC1/Slc25a12 knockout mice contributes to altered visual function. *Mol. Vis.* **22,** 1198–1212 Medline
32. Jalil, M. A., Begum, L., Contreras, L., Pardo, B., Iijima, M., Li, M. X., Ramos, M., Marmol, P., Horiuchi, M., Shimotsu, K., Nakagawa, S., Okubo, A., Sameshima, M., Isashiki, Y., Del Arco, A., *et al.* (2005) Reduced *N*-acetylaspartate levels in mice lacking aralar, a brain- and muscle-type mitochondrial aspartate-glutamate carrier. *J. Biol. Chem.* **280,** 31333–31339 CrossRef Medline
33. Okawa, H., Sampath, A. P., Laughlin, S. B., and Fain, G. L. (2008) ATP consumption by mammalian rod photoreceptors in darkness and in light. *Curr. Biol.* **18,** 1917–1921 CrossRef Medline
34. Salomão, S. R., Berezovsky, A., Andrade, R. E., Belfort, R., Jr., Carelli, V., and Sadun, A. A. (2004) Visual electrophysiologic findings in patients

from an extensive Brazilian family with Leber's hereditary optic neuropathy. *Doc. Ophthalmol.* **108,** 147–155 CrossRef Medline

35. Grönlund, M. A., Honarvar, A. K., Andersson, S., Moslemi, A. R., Oldfors, A., Holme, E., Tulinius, M., and Darin, N. (2010) Ophthalmological findings in children and young adults with genetically verified mitochondrial disease. *Br. J. Ophthalmol.* **94,** 121–127 CrossRef Medline
36. Sadun, A. A., Salomao, S. R., Berezovsky, A., Sadun, F., Denegri, A. M., Quiros, P. A., Chicani, F., Ventura, D., Barboni, P., Sherman, J., Sutter, E., Belfort, R., Jr., and Carelli, V. (2006) Subclinical carriers and conversions in Leber hereditary optic neuropathy: a prospective psychophysical study. *Trans. Am. Ophthalmol. Soc.* **104,** 51–61 Medline
37. Knospe, V., Donoso, L. A., Banga, J. P., Yue, S., Kasp, E., and Gregerson, D. S. (1988) Epitope mapping of bovine retinal S-antigen with monoclonal antibodies. *Curr. Eye Res.* **7,** 1137–1147 CrossRef Medline
38. Travis, A. M., Heflin, S. J., Hirano, A. A., Brecha, N. C., and Arshavsky, V. Y. (2018) Dopamine-dependent sensitization of rod bipolar cells by GABA is conveyed through wide-field amacrine cells. *J. Neurosci.* **38,** 723–732 CrossRef Medline
39. Vinberg, F., Kolesnikov, A. V., and Kefalov, V. J. (2014) *Ex vivo* ERG analysis of photoreceptors using an *in vivo* ERG system. *Vision Res.* **101,** 108–117 CrossRef Medline
40. Sillman, A. J., Ito, H., and Tomita, T. (1969) Studies on the mass receptor potential of the isolated frog retina. I. General properties of the response. *Vision Res.* **9,** 1435–1442 CrossRef Medline
41. Nymark, S., Heikkinen, H., Haldin, C., Donner, K., and Koskelainen, A. (2005) Light responses and light adaptation in rat retinal rods at different temperatures. *J. Physiol.* **567,** 923–938 CrossRef Medline
42. Lobanova, E. S., Herrmann, R., Finkelstein, S., Reidel, B., Skiba, N. P., Deng, W. T., Jo, R., Weiss, E. R., Hauswirth, W. W., and Arshavsky, V. Y. (2010) Mechanistic basis for the failure of cone transducin to translocate: why cones are never blinded by light. *J. Neurosci.* **30,** 6815–6824 CrossRef Medline
43. Sokolov, M., Strissel, K. J., Leskov, I. B., Michaud, N. A., Govardovskii, V. I., and Arshavsky, V. Y. (2004) Phosducin facilitates light-driven transducin translocation in rod photoreceptors. Evidence from the phosducin knockout mouse. *J. Biol. Chem.* **279,** 19149–19156 CrossRef Medline
44. Bownds, D., Gordon-Walker, A., Gaide-Huguenin, A. C., and Robinson, W. (1971) Characterization and analysis of frog photoreceptor membranes. *J. Gen. Physiol.* **58,** 225–237 CrossRef Medline
45. Sokolov, M., Lyubarsky, A. L., Strissel, K. J., Savchenko, A. B., Govardovskii, V. I., Pugh, E. N., Jr., and Arshavsky, V. Y. (2002) Massive light-driven translocation of transducin between the two major compartments of rod cells: a novel mechanism of light adaptation. *Neuron* **34,** 95–106 CrossRef Medline